Spatial coherence effects in second-harmonic generation of scalar light fields

Henri Pesonen[1], Atri Halder[1], Juha-Matti Huusko[2], Ari T. Friberg[1], Tero Setälä[1] and Jari Turunen[1]

[1]Institute of Photonics, University of Eastern Finland, P. O. Box 111, FI-80101 Joensuu, Finland
[2]Department of Physics and Mathematics, University of Eastern Finland, P. O. Box 111, FI-80101 Joensuu, Finland

E-mail: henri.a.pesonen@uef.fi

June 2020

Abstract. We consider the spectral spatial coherence properties of scalar light fields in second-harmonic generation in an optically nonlinear medium. Specifically, we take the fundamental-frequency (incident) field to be a Gaussian Schell-model (GSM) beam with variable peak spectral density and different coherence properties. We show that with increasing intensity the overall degree of coherence of both the fundamental and the second-harmonic field in general decreases on propagation. In addition, the spectral density distributions and the two-point degree of coherence may, for both beams, deviate significantly from those of the GSM, especially at high intensities. Propagation in nonlinear medium is numerically analyzed with the Runge–Kutta and the beam-propagation method of which the latter is found to be considerable faster. The results of this work provide means to synthesize, via nonlinear material interaction, random optical beams with desired coherence characteristics.

1. Introduction

Optical coherence [1, 2] and nonlinear optics [3, 4] are central research areas of modern optics. Both topics are extensive but the influence of partial optical coherence (temporal, spatial, or spectral) in nonlinear light-matter interactions has been analyzed only in a few specific cases. For example, in the context of second-harmonic generation (SHG) the conversion efficiency with an incident spatially [5] and temporally [6] partially coherent beam as well as with astigmatic beams [7] has been considered. Further, the spectral properties of the second-harmonic field induced by a Gaussian Schell-model (GSM) beam [8] and an incoherent conical beam [9] have been investigated. Other researches cover, e.g., the effect of an incoherent pump beam in parametric amplification [10], spatial coherence of local second-harmonic fields at rough metal surfaces [11], pulse propagation in Kerr medium [12], and supercontinuum coherence [13–15].

In this work, we assess, within the scalar-field formalism, the coherence properties of the second-harmonic field produced by a stationary GSM beam in a nonlinear optical material. We use the depleted (incident) beam model that takes into account the effect of the nonlinear interaction on the incident fundamental-frequency GSM beam. Hence, besides the second-harmonic field, we also consider the coherence changes in the fundamental-frequency beam. The random GSM beam in front of the crystal is represented by constructing an ensemble of monochromatic (random-shaped) realizations. Each realization is then propagated through the nonlinear crystal one at a time using the Runge–Kutta (RK) algorithm and the beam-propagation (BP) method tailored for the present context. Both techniques provide highly similar results, but the latter technique is observed to be two orders of magnitude faster. In general, the degrees of coherence of both the fundamental and the second-harmonic wave are found to decrease on propagation. The origin of this effect is the second-harmonic creation at the strongest peaks of the fundamental-wave realizations which increases the structural complexity in the realizations of both fields. The effect is stronger for higher incident-field peak intensities leading to fundamental and second-harmonic fields whose coherence properties may deviate significantly from the GSM. Nonlinear material response can therefore be used to control and tailor the coherence properties of random beams.

This work is organized as follows. In Sec. 2 the GSM beam and its propagation in a nonlinear medium supporting SHG are described. Section 3 is devoted to the numerical analysis on the coherence effects taking place in SHG and Sec. 4 is a summary of the main results. Several theoretical aspects have been relegated to Appendices A-D. In A the construction of an ensemble representing a GSM beam is described. In B and C the RK and BP propagation methods, respectively, are outlined and D evaluates the sufficient number of realizations.

2. Second-harmonic generation with a Gaussian Schell-model beam

In this section we introduce the relevant concepts concerning the GSM beams and their propagation in a nonlinear medium exhibiting SHG.

2.1. Gaussian Schell-model beams

The spatial coherence properties of a stationary scalar light beam at points x_1 and x_2 in a plane $z = z_0$ and at frequency ω are described by the cross-spectral density (CSD) function. The CSD can be defined as [1]

$$W(x_1, x_2, z_0; \omega) = \langle E^*(x_1, z_0; \omega) E(x_2, z_0; \omega) \rangle, \qquad (1)$$

where the asterisk denotes complex conjugation and the angular brackets refer to ensemble averaging. In addition, $E(x, z_0; \omega)$ is a monochromatic field realization representing a random electric field which in this work is taken to be linearly polarized. Also the field generated in nonlinear interaction is similarly linearly polarized allowing a scalar treatment of all fields. In this section, we drop the explicit frequency and z dependencies for notational simplicity and assume that the formulas are given at the entrance facet of a nonlinear crystal. By setting $x_1 = x_2 = x$ we obtain the (average) spectral density of the field as $S(x) = W(x, x)$. The normalized CSD, namely the complex (spectral) degree of spatial coherence, reads

$$\mu(x_1, x_2) = \frac{W(x_1, x_2)}{\sqrt{S(x_1) S(x_2)}}. \qquad (2)$$

It is known that the CSD admits the coherent-mode representation [1, 2], i.e., an expansion in terms of the

mutually uncorrelated, spatially fully coherent modes. This is explicitly given by

$$W(x_1, x_2) = \sum_{m=0}^{\infty} \alpha_m \psi_m^*(x_1)\psi_m(x_2), \tag{3}$$

where the weights α_m are real and nonnegative and the mode functions $\psi_m(x)$ are orthonormal in the considered region. The eigenvalues and eigenfunctions are solutions of a Fredhold integral equation [1]. For a GSM beam the mode functions are of Hermite-Gaussian (HG) form, written as [1,16]

$$\psi_m(x) = \frac{(2/\pi)^{1/4}}{\sqrt{2^m m! w_0}} H_m\left(\frac{\sqrt{2}x}{w_0}\right) \exp\left(-\frac{x^2}{w_0^2}\right), \tag{4}$$

while the modal weights are

$$\alpha_m = S_0 \sqrt{\frac{2\pi}{\beta}} \frac{w_0}{1+1/\beta} \left(\frac{1-\beta}{1+\beta}\right)^m. \tag{5}$$

Above, S_0 is the (spatial) peak spectral density, w_0 represents the mode width, and $H_m(x)$ is a Hermite polynomial. Parameter β is a real constant ranging between $0 \leq \beta \leq 1$ and it connects the width w of the GSM beam and w_0 as $w = w_0/\sqrt{\beta}$.

The full CSD of a GSM beam can be expressed as

$$W(x_1, x_2) = S_0 \exp\left(-\frac{1+\beta^2}{2\beta}\frac{x_1^2 + x_2^2}{w_0^2}\right) \times \exp\left(\frac{1-\beta^2}{\beta}\frac{x_1 x_2}{w_0^2}\right), \tag{6}$$

and the related spectral density is

$$S(x) = S_0 \exp\left(-\frac{2x^2}{w^2}\right). \tag{7}$$

These enable us to write the complex degree of coherence of Eq. (2) in the form

$$\mu(x_1, x_2) = \exp\left[-\frac{(x_2 - x_1)^2}{2\sigma^2}\right], \tag{8}$$

where $\sigma = \sqrt{\beta/(1-\beta)}w_0$ describes the coherence width of the GSM beam. We further introduce the overall (effective) degree of coherence [17,18]

$$\bar{\mu}^2 = \frac{\int_{-\infty}^{\infty}\int_{-\infty}^{\infty} |W(x_1, x_2)|^2 \mathrm{d}x_1 \mathrm{d}x_2}{\int_{-\infty}^{\infty}\int_{-\infty}^{\infty} S(x_1)S(x_2)\mathrm{d}x_1\mathrm{d}x_2}, \tag{9}$$

which characterizes the intensity-weighted degree of spatial coherence. For a GSM beam, $\bar{\mu} = \sqrt{\beta}$ holds.

2.2. Propagation in nonlinear medium

In this work, a GSM beam is propagated through a nonlinear medium one realization $E(x, z; \omega)$ at a time. The construction of a statistical ensemble of realizations that represents a GSM beam is described in Appendix A. We assume that the medium is nonmagnetic, source free, and its (dispersive) linear response is isotropic. The nonlinear response of the medium is taken local and its strength is expressed by the nonlinear susceptibility d (in contracted notation) under the Kleinman symmetry conditions. We from now on refer to field $E(x, z; \omega)$ as the fundamental (F) wave and invoke the notation $E_1(x, z) = E(x, z; \omega_1)$. The second-harmonic (SH) wave at frequency $\omega_2 = 2\omega_1$ generated in the medium is denoted by $E_2(x, z)$. The two waves are coupled in propagation and obey [3]

$$\nabla^2 E_1(x, z) + k_1^2 E_1(x, z) = -4\frac{d\omega_1^2}{c^2} E_1^*(x, z) E_2(x, z), \tag{10}$$

$$\nabla^2 E_2(x, z) + k_2^2 E_2(x, z) = -2\frac{d\omega_2^2}{c^2} E_1^2(x, z), \tag{11}$$

where $k_i = n(\omega_i)\omega_i/c$ with $n(\omega_i)$ being the refractive index, $i \in (1, 2)$, and c is the vacuum speed of light.

The above coupled equations are numerically solved by employing the RK method outlined in Appendix B and the BP method described in Appendix C. We compared these methods in the context of field propagation in a nonlinear medium. The implementation is with Matlab and the two methods rely on the available RK and Fast Fourier Transform (FFT) algorithms. As an example, with 600 and 20000 sampling points in the transverse and longitudinal directions, respectively, the calculation times were 165.5 s with the RK and 0.7 s with the BP method. Thus, the BP method can here be regarded as two orders of magnitude faster than the RK technique. As an example, in Appendix C the output spectral density distributions of the F and SH waves computed with the two methods are considered in a specific case. It is verified that with high accuracy the methods lead to identical results.

We notice that different ensembles can produce different SH-field coherence properties since the input F-field realizations themselves affect the generated SH field realizations via nonlinear interaction. We assessed this possible effect by calculating the coherence properties of the F and SH fields at the output of the nonlinear crystal for several ensembles of realizations. It turned out that for sufficiently large ensembles the SH-wave coherence properties were effectively the same for all sets. The same holds for the F waves. These are important justifications for the validity of the method. The influence of the number of members in an ensemble is considered in Appendix D. It is found that the coherence properties reach convergence (are essentially unaltered if more realizations are included) when the number of realizations exceeds about three hundred.

3. Numerical results

In this section we evaluate numerically the spatial coherence properties of the F and SH beams propagating in a nonlinear medium. We employ the

BP method for field propagation as it was confirmed to be significantly faster than the RK technique. The incident (F) field is a linearly (fully) polarized GSM beam at frequency ω_1. In the entrance facet of the crystal (chosen to be at $z = 0$) the field is represented by a set of realizations $\{E_{1n}(x, 0)\}$ whose construction is explained in Appendix A. Averaging over all realizations leads to the CSD of Eq. (6) as well as to the Gaussian spectral density of Eq. (7) and the degree of coherence described by Eq. (8). The width of the incident beam is in all considered cases fixed at $w = w_0/\sqrt{\beta} = 40\lambda_1$ with the (vacuum) wavelength of the F wave being $\lambda_1 = 0.8$ μm. The effective degree of coherence of the incident beam is varied by taking $\beta \in \{0.3, 0.5, 0.7, 0.85, 0.97\}$, where the extremes correspond to a weakly and highly coherent beams, respectively. We do not consider lower β values since the beam width is $40\lambda_1$ and the transverse coherence length is in practise at least a few wavelengths. For each β value, we consider the spectral densities specified by $\sqrt{S_0} \in$ [0.001 GV/m, 0.8 GV/m]. This accordingly affects the amplitudes of the individual realizations in the ensemble and stronger amplitudes are expected to imply more notable nonlinear effects. Furthermore, we choose the length L of the crystal as $L = 0.5$ mm and take the medium to be such that the F and SH waves have the same linear polarization state which is preserved on propagation. Hence, the nonlinear susceptibility has only one nonzero element whose value is taken as $d = 2.0 \times 10^{-12}$ m/V. All the parameters are chosen such that measurements are possible, at least in principle, with a picosecond pulse laser, for instance.

In the following we consider two cases. First, the refractive index of the crystal is the same at both frequencies, $n(\omega_1) = n(\omega_2) = 1.66$. Second, the indices are different, $n(\omega_1) = 1.660$, $n(\omega_2) = 1.661$. We refer to these situations as the "phase-matched case" and the "phase-mismatched case", respectively. We ignore the back reflections at the output facet as the related reflectance for the slab with chosen indices (surrounded by air) is a few percent at normal incidence.

3.1. Phase-matched case

Taking the refractive indices the same at the two frequencies, we calculate the squared overall degree of coherence for both the F and SH beams as a function of incident beam's $\sqrt{S_0}$, which is a measure for the average peak amplitude. The computations are carried out for several β values and the results are shown in Fig. 1. The pink, yellow, blue, green, and orange curves refer to the β values of 0.3, 0.5, 0.7, 0.85, and 0.97, respectively. In addition, the solid lines indicate the F waves whereas the dashed lines denote the SH beam. We note that with small incident-field amplitudes, the degree of coherence of the F field does not change upon propagation. This is explained by the facts that the propagation distance is short and the low amplitude does not induce significant SHG.

We further see from Fig. 1 that when $\sqrt{S_0}$ is increased, the effective degree of coherence of the F beam reduces rapidly for all β. At the same time, the SH beam's $\bar{\mu}$ remains nearly constant. Consequently, for all β values, the SH beam's degree of coherence at some point becomes larger than that of the F beam. This subsequently holds within a certain amplitude range which is the wider the higher is the incident F wave β value. For $\beta = 0.85$ the range extends roughly from 0.12 GV/m to 0.5 GV/m and is marked in Fig. 1 with green area. Near the end of the range the overall degree of coherence of the F beam increases slightly which is followed by a notable decrease in $\bar{\mu}$ of the SH beam. The above features can be explained by considering the behavior of the individual realizations as will be seen shortly. It is also observed that for high $\sqrt{S_0}$ values the output $\bar{\mu}$ of both beams is significantly smaller that that at the entrance facet. As an example, for the F wave with $\beta = 0.85$ the overall degree of coherence drops from $\sqrt{0.85} \approx 0.92$ to about $\sqrt{0.08} \approx 0.28$. Hence, interaction with a

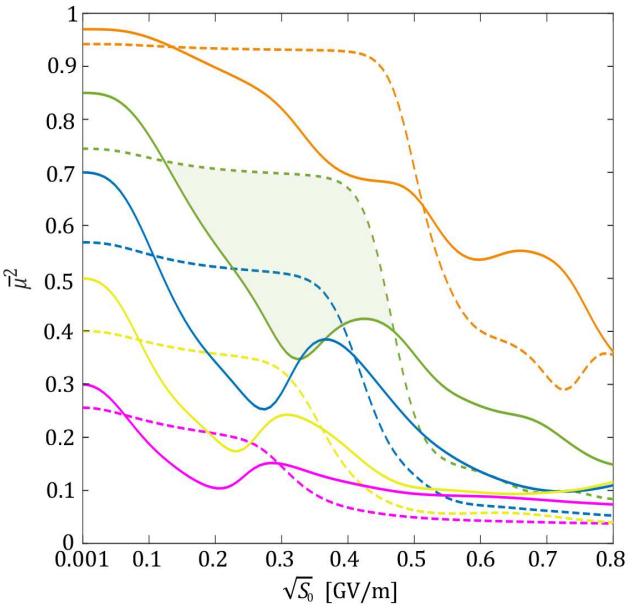

Figure 1. The squared effective degree of coherence of the F (solid lines) and SH (dashed lines) beams propagated through a nonlinear crystal as a function of the incident beam's $\sqrt{S_0}$. The pink, yellow, blue, green, and orange curves correspond, respectively, to $\beta = \{0.3, 0.5, 0.7, 0.85, 0.97\}$ of the incident GSM beam. For the case of $\beta = 0.85$ the region where the SH beam $\bar{\mu}$ is larger than that of the F wave is shaded with green. The various beam and medium parameters are: $\lambda_1 = 0.8$ μm, $w = 40\lambda_1$, $L = 0.5$ mm, $d = 2.0 \times 10^{-12}$ m/V, and $n(\omega_1) = n(\omega_2) = 1.66$.

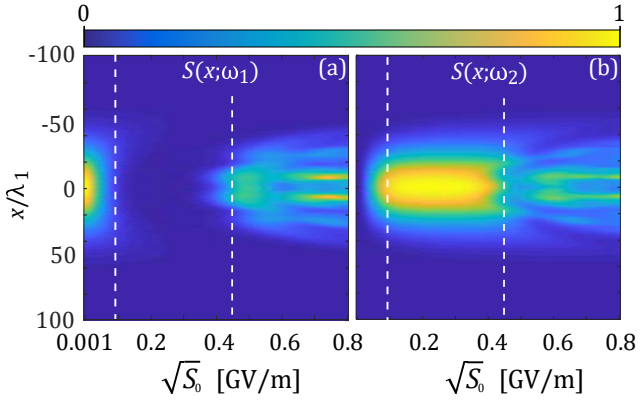

Figure 2. Normalized spectral density distributions of (a) the F field and (b) the SH beam, at the output facet of a nonlinear crystal as a function of $\sqrt{S_0}$. The normalization factor is $S(0)$ at $\sqrt{S_0} = 0.001$ GV/m. The β value of the incident GSM beam is set to 0.85 and the white dashed lines correspond to the examples discussed in Fig. 3. Other material and field parameters are as in Fig. 1.

nonlinear optical material provides a way to render a highly coherent beam into weakly coherent.

The normalized spectral densities of the F and SH beams at the crystal output are shown in Figs. 2(a) and (b) as a function of $\sqrt{S_0}$ in the case of $\beta = 0.85$. Each vertical slice corresponds to a fixed $\sqrt{S_0}$ value. The figures illustrate the coupling of the F-beam and SH-beam energies on propagation. The meaning of the white dashed lines will be explained later. By comparing the spectral density distributions with the overall degrees of coherence of Fig. 1, it is evident that a range of almost constant $\bar{\mu}$ of the SH beam takes place when most of the F-beam energy has been transferred to the SH beam. In contrast, at $0.4 - 0.5$ GV/m, where the abrupt decrease of the degree of coherence of the SH field occurs, the F-wave total output energy is larger than that of the SH field. In general, for a fixed crystal length the output energy oscillates between the F and SH fields as a function of $\sqrt{S_0}$. This behavior is similar to what has been found as a function of the propagation distance in works assessing the efficiency of SHG [3, 19].

To explain the behavior of the overall degree of coherence of the SH beam we consider an ensemble of the incident GSM-beam realizations. Averaging over all realizations produces a Gaussian spectral density distribution. However, individual realizations are not necessarily Gaussian. In particular, when the beam is partially coherent the realizations exhibit random spatial shape possibly with several intensity peaks. The lower the overall degree of coherence, the more random structure the realizations in general show. For a single realization the SHG is strongest at the locations of high intensity. For a low $\sqrt{S_0}$ value only the strongest intensity peak in a realization is able to contribute significantly to the SH-wave realization whose shape consequently exhibits a peak at this position. The spatial locations of these peaks in the SH realizations are highly randomly distributed and represent a field which is less coherent than the F field. This explains why for small $\sqrt{S_0}$ values $\bar{\mu}$ is smaller for the SH beam in Fig. 1.

When $\sqrt{S_0}$ increases more peaks in an F wave realization can contribute to the SHG and randomness in the SH-field realizations increases. This tends to decrease the overall degree of coherence of the SH field as a function of $\sqrt{S_0}$ as observed in Fig. 1. Simultaneously, the peaks in the F-field realizations contributing to the SHG are split into two as the energy in the middle of a peak is transferred to the SH-field realization. This effect increases the number of peaks in the F-wave realizations and likewise leads to a decreasing trend in $\bar{\mu}$. The abrupt decrease of the SH-field $\bar{\mu}$ occurs when $\sqrt{S_0}$ becomes sufficiently large to induce SHG also in the tail parts of the F-field realizations. In this case, the SH (and F) realizations show highly peaked (random) structures and also lead to the filamentation of the spectral density distributions as observed in the right-hand sides of Figs. 2(a) and (b).

Figures 3(a) and (b) show the spectral density distributions of the F field (blue solid curve) and the SH field (orange solid curve) along the white dashed lines located at 0.09 GV/m and 0.45 GV/m, respectively, in Fig. 2. Black dashed lines depict the incident-wave Gaussian spectral density whose peak value is used to normalize all the curves. In Fig. 3(a) the dip in the middle part of the F-beam curve demonstrates the energy transfer to the SH beam which displays nearly Gaussian shape whereas the

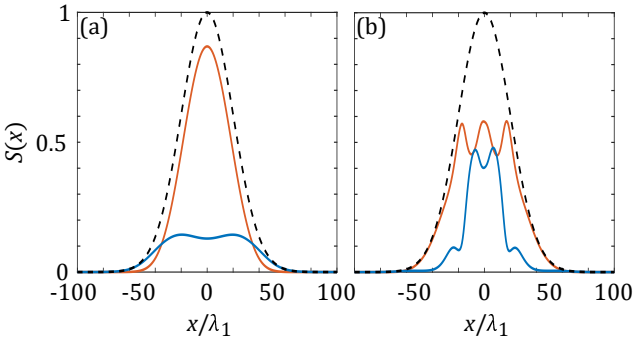

Figure 3. Distributions of the transmitted spectral densities of the F (blue solid curve) and SH (orange solid curve) beams in the cases of (a) $\sqrt{S_0} = 0.09$ GV/m and, (b) $\sqrt{S_0} = 0.45$ GV/m. Black dashed curves show the incident Gaussian spectral density. The situations in (a) and (b), respectively, correspond to the left and right white dashed lines in Figs. 2(a) and (b). All curves have been normalized with S_0.

filamentation of both beams is visible in (b). Hence, due to the nonlinear optical response of the medium both the F and SH output beams may, at large incident intensities, deviate significantly from a Gaussian shape. Notice also that in the cases of (a) and (b) the overall SH-field degree of coherence is in the flat and rapidly decreasing regions in Fig. 2 (green dashed curve). By comparing the spectral density distributions of the incident and transmitted beams we further observe that the widths are similar for all beams in (a) but in (b) the width of the transmitted F beam is half of that of the SH beam. This suggests that a nonlinear light-matter interaction could be exploited to synthesize a beam with adjustable (narrower) width.

Figure 4 presents the magnitude of the degree of coherence at the output of a nonlinear crystal for the F beam (left column) and the SH beam (right column). The upper row corresponds to the low amplitude case of $\sqrt{S_0} = 0.09$ GV/m whereas the lower row represents the high amplitude situation with $\sqrt{S_0} = 0.45$ GV/m, which both are also depicted with vertical white dashed lines in Fig. 2. As seen from 4(a), even with a low incident-field amplitudes the degree of spatial coherence of the F beam deviates notably from that of the original GSM beam (which would be a straight diagonal bar but not shown). The origin of this

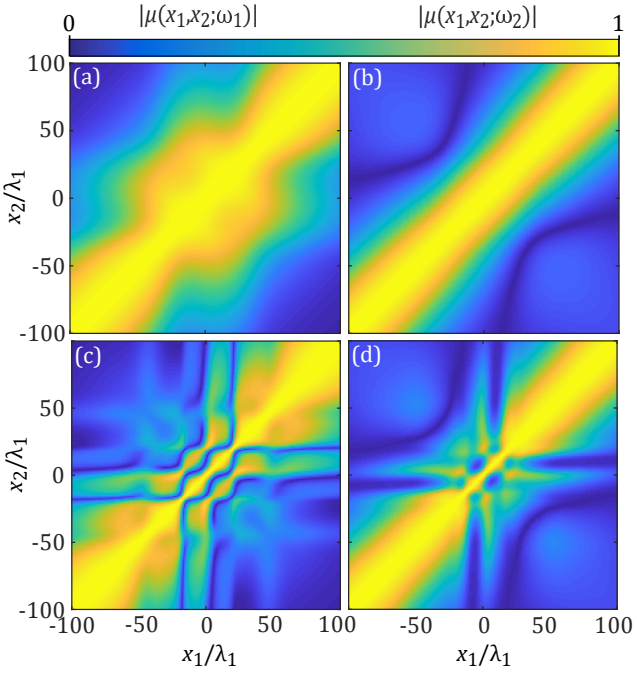

Figure 4. Magnitudes of the degree of coherence of the F beam (left column) and SH beam (right column) at the output facet of a nonlinear crystal for $\beta = 0.85$ of the incident GSM beam. The upper and lower rows correspond to the cases of $\sqrt{S_0} = 0.09$ GV/m and $\sqrt{S_0} = 0.45$ GV/m, respectively, marked with white dashed lines in Fig. 2.

modulation can be traced to the splitting of the F-field realizations as discussed earlier. In contrast, as seen from (b) the SH beam degree of coherence resembles the GSM beam coherence. At high intensities and for both beams the degree of coherence becomes strongly modulated as is visible in (c) and (d). The modulation is particularly strong in the region of high spectral density extending roughly from $-40\lambda_1$ to $40\lambda_1$ [see Figs. 3(a) and (b)]. The above observations suggest that SHG can be employed to alter and control the two-point spatial coherence properties of light beams.

3.2. The phase-mismatched case

Next we assess the situation in which the refractive index is different at different frequencies. We choose $n(\omega_1) = 1.660$ and $n(\omega_2) = 1.661$ which amount to a (dispersive) phase mismatch of $\Delta k = 2k_1 - k_2 = -1.5708 \times 10^4$ rad/m (for collinear components). The other parameters are as in Sec. 3.1. The phase mismatch is expected to reduce the efficiency of the SHG which is clearly visible in Figs. 5(a) and (b) showing the output spectral density distributions for the F and SH beams, respectively, as a function of $\sqrt{S_0}$. In addition, the SHG occurs periodically as function of $\sqrt{S_0}$. Analogous phase-mismatch-induced periodicity of the F- and SH-wave energies but as a function of the propagation distance has been discussed, e.g., in Refs. [3, 19].

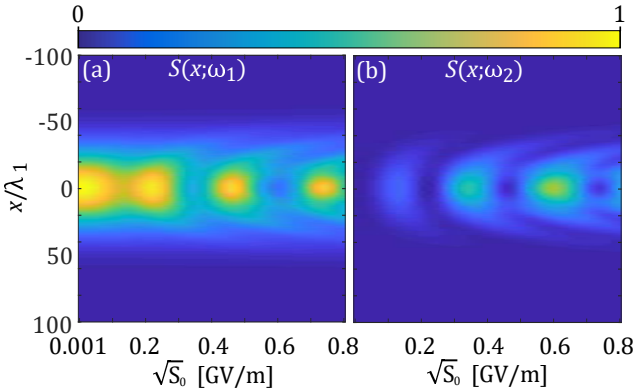

Figure 5. Same as in Fig. 2, but for $n(\omega_1) = 1.660$ and $n(\omega_2) = 1.661$.

The overall degree of coherence as a function of $\sqrt{S_0}$ is presented in Fig. 6 in the cases of $\beta \in \{0.3, 0.5, 0.7, 0.85, 0.97\}$ with pink, yellow, blue, green, and orange lines, respectively. The solid lines refer to the F beam while the dashed lines represent the SH field. For both beams the degree in general decreases with increasing $\sqrt{S_0}$. The mechanism behind this behavior is the same as in the phase-matched case of Fig. 1, i.e., more intensity peaks in the random

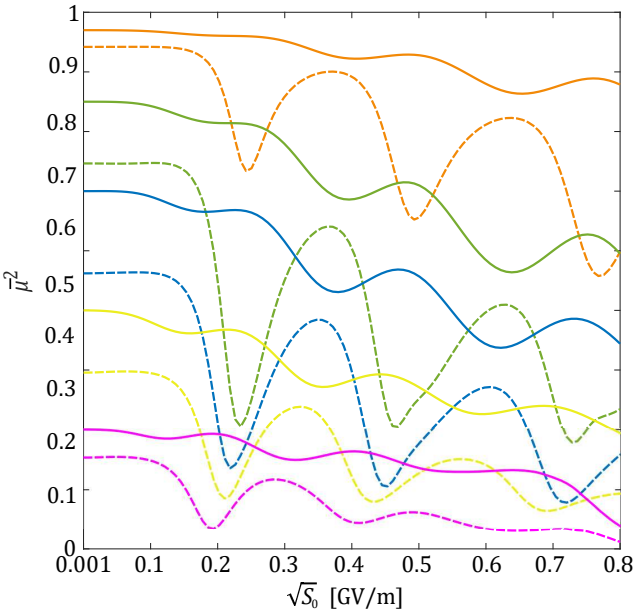

Figure 6. Same as in Fig. 1, but for $n(\omega_1) = 1.660$ and $n(\omega_2) = 1.661$.

realizations contribute to SHG while the intensity peaks of F-field realizations are split. Further, by comparing Figs. 5 and 6 we observe that the local maxima of the spectral density coincide with the maxima of the $\bar{\mu}$ curves for both beams. The periodic oscillations in the spectral density and the overall degree of coherence as a function of $\sqrt{S_0}$ originate from the phase mismatch. Similar effects are not present in Figs. 1 and 2.

4. Conclusions

We analysed the spectral spatial coherence effects in SHG induced by a stationary GSM beam. The overall degrees of coherence of the F and SH fields at the exit facet of a nonlinear crystal were found to decrease significantly with increasing peak intensity of the incident beam. In particular, at strong intensities, a highly coherent GSM beam may generate a weakly coherent SH beam and become highly incoherent itself on propagation. Hence the SHG effect can be used to render a coherent beam into a weakly coherent one. In addition, the coherence properties of both fields may significantly differ from the GSM, especially at high F-wave intensities. In particular, the spectral density distributions of both F and SH waves may show filament structures or the F wave width may be significantly smaller than that of the incident GSM beam. Further, the two-point degree of coherence can be modified to deviate significantly from a Gaussian shape. Propagation in nonlinear medium was performed with the RK and BP methods which led to identical results but the latter was found to be two orders of magnitude faster. The results suggest that the coherence properties of light beams can be tailored and controlled by exploiting a nonlinear material interaction.

Appendix A. Construction of an ensemble of realizations

In this appendix we construct an ensemble of realizations describing a GSM beam. Specifically, we require that the CSD is of the form of Eq. (3) with the modes $\psi_m(x)$ given by the HG functions of Eq. (4). We write a single realization as

$$E_n(x) = \sum_{m=0}^{M-1} \alpha'_{nm} \psi_m(x), \tag{A.1}$$

where M is a sufficiently large number and α'_{nm} are random complex numbers to be determined. Averaging over the ensemble as in Eq. (1) results in

$$W(x_1, x_2) = \sum_{m=0}^{M-1} \sum_{m'=0}^{M-1} \left(\frac{1}{N} \sum_{n=0}^{N-1} \alpha'^{*}_{nm} \alpha'_{nm'} \right) \times \psi^*_m(x_1) \psi_{m'}(x_2), \tag{A.2}$$

where we assumed that the ensemble contains N realizations. Theoretically both N and M should approach infinity but in practise the summations have to be cut as we have done. For Eq. (A.2) to coincide with the CSD of a GSM the following must hold

$$\frac{1}{N} \sum_{n=0}^{N-1} \alpha'^{*}_{nm} \alpha'_{nm'} = \alpha_m \delta_{mm'}, \tag{A.3}$$

where α_m is the modal coefficient given in Eq. (5) and $\delta_{mm'}$ is the Kronecker delta function. We may set

$$\alpha'_{nm} = \sqrt{\alpha_m} \exp(i\phi_{nm}), \tag{A.4}$$

where ϕ_{nm} is a random phase uniformly distributed within the interval $[0, 2\pi]$. Equations (A.3) and (A.4) therefore imply

$$\frac{1}{N} \sum_{n=0}^{N-1} \exp[i(\phi_{nm'} - \phi_{nm})] = \delta_{mm'}. \tag{A.5}$$

Next we introduce the phase matrix

$$\boldsymbol{\phi} = \begin{pmatrix} \exp(i\phi_{00}) & \dots & \exp[i\phi_{0(M-1)}] \\ \exp(i\phi_{10}) & \ddots & \\ \vdots & & \\ \exp[i\phi_{(N-1)0}] & & \exp[i\phi_{(N-1)(M-1)}] \end{pmatrix}, \tag{A.6}$$

whose rows represent individual realizations and columns are mutually orthogonal vectors if M is infinitely large. However, since M is finite we

employ the Gram-Schmidt method to render them orthonormal. This then leads to a matrix

$$\mathbf{C} = \begin{pmatrix} c_{00} & \cdots & c_{0(M-1)} \\ c_{10} & \ddots & \\ \vdots & & \\ c_{(N-1)0} & & c_{(N-1)(M-1)} \end{pmatrix}, \tag{A.7}$$

whose columns are orthonormal vectors and satisfy

$$\frac{1}{N}\sum_{n=0}^{N-1} c_{nm}^{*} c_{nm'} = \delta_{mm'}. \tag{A.8}$$

We then set

$$\alpha'_{nm} = \sqrt{\alpha_m}\, c_{nm}, \tag{A.9}$$

which via Eq. (A.1) generates an ensemble of random realizations that represents a GSM beam. We point out that, e.g., in Refs. [8–10, 12] the above orthonormalization procedure was not employed and hence the resulting CSD may not accurately represent a GSM beam.

Appendix B. Runge–Kutta method

Below we describe the main points of the RK propagation method. We invoke the envelope representation of the field as $E_j(x,z) = A_j(x,z)\exp(ik_j z)$ and for expressing the required formulas we introduce a new variable $A'_j(x,z) = \partial_z A_j(x,z)$ with $\partial_z = \partial/\partial_z$, $j \in (1,2)$. This allows us to split the second-order z derivatives in Eqs. (10) and (11) into four first-order derivatives leading to

$$\partial_z A_1(x,z) = A'_1(x,z), \tag{B.1}$$

$$\begin{aligned}\partial_z A'_1(x,z) = & -4\frac{d\omega_1^2}{c^2} A_1^{*}(x,z) A_2(x,z)\exp(-i\Delta k z) \\ & - i2k_1 A'_1(x,z) - \partial_{xx} A_1(x,z),\end{aligned} \tag{B.2}$$

$$\partial_z A_2(x,z) = A'_2(x,z), \tag{B.3}$$

$$\begin{aligned}\partial_z A'_2(x,z) = & -2\frac{d\omega_2^2}{c^2} A_1^{2}(x,z)\exp(i\Delta k z) \\ & - i2k_1 A'_2(x,z) - \partial_{xx} A_2(x,z),\end{aligned} \tag{B.4}$$

where $\partial_{xx} = \partial^2/\partial x^2$ and $\Delta k = 2k_1 - k_2$ are the spatial second-order derivative and the phase mismatch, respectively. The set of Eqs. (B.1)–(B.4) can be integrated with respect to z by employing the RK algorithm [20]. When using an ordinary differential equation solver one needs to perform the spatial second order derivations numerically on every integration step. We also employ a nonlinear coordinate transformation [21] to prevent the reflections from the calculation window boundaries.

Appendix C. Beam-propagation method

Next we outline the BP method [22] for field propagation in a nonlinear medium. The solutions for the homogeneous versions of Eqs. (10) and (11) can be written using the angular-spectrum representation as [23]

$$E_j(k_{xj},z) = \frac{1}{2\pi}\int_{-\infty}^{\infty} E_j(x,z)\exp(-ik_{xj}x)\mathrm{d}x, \tag{C.1}$$

$$\begin{aligned}E_j(x,z) = & \int_{-\infty}^{\infty} E_j(k_{xj},z_0) \\ & \times \exp(ik_{xj}x + ik_{zj}\Delta z)\mathrm{d}k_{xj},\end{aligned} \tag{C.2}$$

where $j \in (1,2)$ and k_{xj} is the spatial frequency, i.e., the wave vector x component, and $\Delta z = z - z_0$ is the propagation step from an arbitrary reference plane at z_0 to z. The z component of the wave vector is $k_{zj} = (k_j^2 - k_{xj}^2)^{1/2}$ for $j \in (1,2)$. To find an expression when the source terms (right-hand sides) are included in Eqs. (10) and (11), we assume that within a small propagation distance Δz the nonlinear polarization changes linearly and its spatial spreading is negligible. Consequently, we may use the slowly-varying envelope approximation (SVEA) [3, 24] and write

$$\nabla^2 E_j(x,z) + k_j^2 E_j(x,z) \approx i2k_j\partial_z A_j(x,z), \tag{C.3}$$

where we have denoted the slowly varying envelope by $A_j(x,z)$, $j \in (1,2)$. We neglected the phase terms $\exp(ik_{zj}z)$ in Eq. (C.3) since the aim is to use the angular-spectrum representation for the field $E_j(x,z)$ that includes the phase. Equating the right-hand side of Eq. (C.3) with those of Eqs. (10) and (11), integrating from z_0 to z, rearranging and combining with Eq. (C.2) yields

$$\begin{aligned}\int_{-\infty}^{\infty} & E_1(k_{x1},z_0)\exp[i(k_{x1}x + k_{z1}\Delta z)]\mathrm{d}k_{x1} \\ & = \frac{2id\omega_1^2}{k_1c^2} E_1(x,z_0)E_2^{*}(x,z_0)\Delta z,\end{aligned} \tag{C.4}$$

$$\begin{aligned}\int_{-\infty}^{\infty} & E_2(k_{x2},z_0)\exp[i(k_{x2}x + k_{z2}\Delta z)]\mathrm{d}k_{x2} \\ & = \frac{id\omega_2^2}{k_2c^2} E_1^{2}(x,z_0)\Delta z.\end{aligned} \tag{C.5}$$

Above, the F and SH fields in the z_0 plane are known and using Eq. (C.1), one can construct, by employing the FFT, an iterative method for the propagation of the coupled fields.

We tested the numerical methods presented in Appendices B and C by propagating a deterministic Gaussian beam whose width and peak amplitude are $w_0 = 20\lambda_1$ and $A_1(0,0) = 1\times10^9$ V/m, respectively, through a second-order nonlinear crystal with the coupling constant $d = 2.0\times10^{-13}$ m/V and thickness $L = 1$ mm. In a plane-wave model the chosen peak amplitude corresponds to the power

of 100 GW/cm^2 which is easily achieved, e.g., with picosecond pulsed lasers. Such long pulses can be regarded stationary conforming with the assumptions of this work. With 600 and 20000 sampling points in the x and z directions, respectively, the calculation times were 165.5 s (RK) and 0.7 s (BP). Therefore, we may consider the BP method two orders of magnitude faster than the RK technique. Figure C1(a) shows the F and SH waves after propagation in the medium. The incident beam profile is shown with black dashed line whereas solid lines present, respectively, the F (red) and the generated SH (yellow) beams calculated with the RK method. The corresponding spectral densities obtained with the BP method are displayed with purple (F) and green (SH) dashed lines. The results are, to a good accuracy, identical.

Appendix D. Convergence arguments

In this appendix we assess the convergence of the results by considering the influence of the number of realizations in an ensemble. As a quantitative measure we employed the overall degree of coherence squared whose values at the nonlinear crystals's exit facet are shown in Fig. C1(b) as a function of the number of realizations. The squares and circles refer to the F and SH waves, respectively, with blue and red colors associated with an incident beam of $\beta = 0.85$, whereas black and magenta represent the situation of $\beta = 0.3$. The incident average amplitude corresponds to the high-intensity case of 0.45 GV/m, which is numerically challenging since both field distributions decompose into narrow filaments. However, in all cases we observe that the overall degree of coherence does not significantly change if the number of realizations exceeds, say, three hundred.

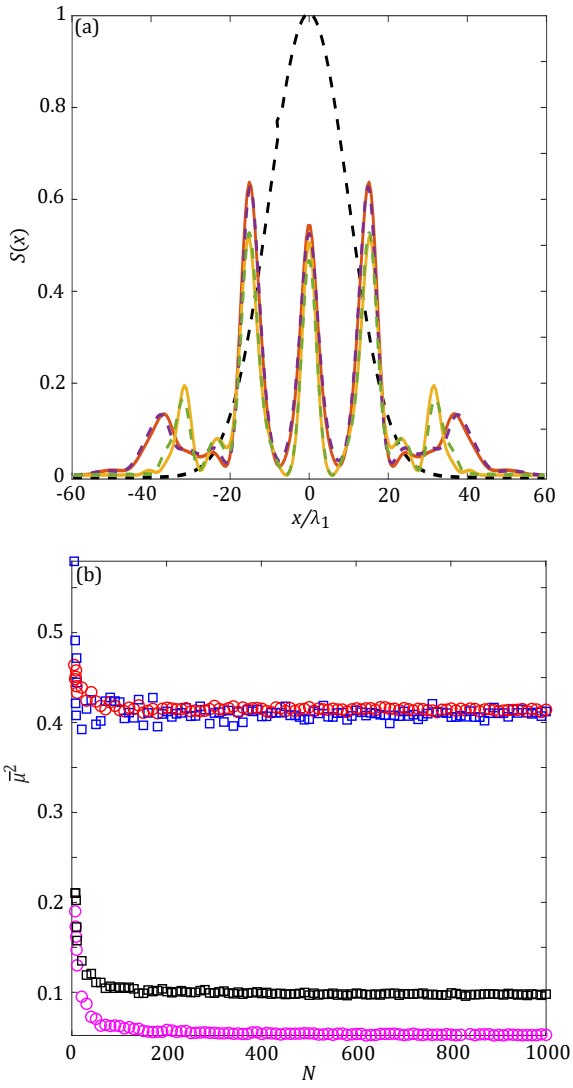

Figure C1. (a) Comparison of the RK and BP methods. Spectral density distributions are shown for the F and SH waves at the output facet of a nonlinear crystal calculated with the RK method [red (F) and yellow (SH) solid lines] and the BP method [purple (F) and green (SH) dashed lines]. The black dashed curve illustrated the incident beam. (b) The squared overall degree of spatial coherence for the F (squares) and SH (circles) waves as a function on the number of realizations. The red and blue symbols denote the case when the initial GSM beam has $\beta = 0.85$, while black and magenta correspond to an incident beam of $\beta = 0.3$. In both cases, the incident beam's average amplitude is 0.45 GV/m.

Acknowledgements

Academy of Finland (projects 285880, 308393, and 310511). This work is part of the Academy of Finland Flagship Program, Photonics Research and Innovation (PREIN, project 320166).

References

[1] Mandel L and Wolf E 1995 *Optical Coherence and Quantum Optics* (Cambridge: Cambridge University Press)
[2] Korotkova O 2014 *Random Light Beams: Theory and Applications* (Boca Raton: CRC Press)
[3] Boyd R W 2008 *Nonlinear Optics* 3rd ed (Amsterdam: Elsevier)
[4] Agrawal P A 1995 *Nonlinear Fiber Optics* 2nd ed (San Diego: Academic Press)
[5] Zubairy M S and McIver J K 1987 Second-harmonic generation by a partially coherent beam *Phys. Rev. A* **36** 202–6
[6] Ji L *et al.* 2019 High-efficiency second-harmonic generation of low-temporal-coherent light pulse *Opt. Lett.* **44** 4359–62
[7] Cai Y and Peschel U 2007 Second-harmonic generation by an astigmatic partially coherent beam *Opt. Express* **15** 15480–92
[8] Pyragaite V, Stabinis A and Piskarskas A 2012 Frequency spectrum of second-harmonic radiation exited by a Gaussian Schell-model beam *Phys. Rev. A* **86** 033812
[9] Stanislovaitis P, Narmontas A, Pyragaite V and Smilgevičius V 2014 Generation of a second-harmonic beam from incoherent conical beams *Phys. Rev. A* **89** 043821

[10] Pyragaite V, Smilgevičius V, Butkus R, Stabinis A and Piskarskas A 2013 Conversion of broadband incoherent pump to narrowband signal in an optical parametric amplifier *Phys. Rev. A* **88** 023820
[11] Stockman M I, Bergman D J, Anceau C, Brasselet S and Zyss J 2004 Enhanced second-harmonic generation by metal surfaces with nanoscale roughness: nanoscale dephasing, depolarization, and correlations *Phys. Rev. Lett.* **92** 057402
[12] Lajunen H, Torres-Company V, Lancis J, Silvestre E and Andrés P 2010 Pulse-by-pulse method to characterize partially coherent pulse propagation in instantaneous nonlinear media *Opt. Express* **18** 14979–91
[13] Genty G, Surakka M, Turunen J and Friberg A T 2010 Second-order coherence of supercontinuum light *Opt. Lett.* **35** 3057–9
[14] Halder A, Jukna V, Koivurova M, Dubietis A and Turunen J 2019 Coherence of bulk-generated supercontinuum *Phot. Res.* **7** 1345–53
[15] Närhi M, Turunen J, Friberg A. T. and Genty G 2016 Experimental measurement of the second-order coherence of supercontinuum *Phys. Rev. Lett.* **116** 243901
[16] Ding C, Koivurova M, Setälä T, Turunen J and Friberg A T 2019 Spectral invariance and scaling law for nonstationary optical fields *Phys. Rev. A* **101** 033808
[17] Bastiaans M J 1984 New class of uncertainty relations for partially coherent light *J. Opt. Soc. Am. A* **1** 711–15
[18] Blomstedt K, Setälä T and Friberg A T 2007 Effective degree of coherence: general theory and application to electromagnetic fields *J. Opt. A: Pure Appl. Opt.* **9** 907–19
[19] Armstrong J A, Bloembergen N, Ducuing J and Pershan P S 1962 Interactions between light waves in a nonlinear dielectric *Phys. Rev.* **127** 1918–39
[20] Butcher J C 2016 *Numerical Methods for Ordinary Differential Equations* 3rd ed (Chichester: John Wiley & Sons)
[21] Hugonin J P and Lalanne P 2005 Perfectly matched layers as nonlinear coordinate transforms: a generalized formalization *J. Opt. Soc. Am. A* **22** 1844–49
[22] Feit M D and Fleck J A 1978 Light propagation in graded-index optical fibers *Appl. Opt.* **17** 3990–8
[23] Goodman J W 2005 *Introduction to Fourier Optics* 3rd ed (Englewood: Roberts & Company)
[24] Trebino R 2000 *Frequency-Resolved Optical Grating: the Measurement of Ultrashort Laser Pulses* (Boston: Springer)